ACS APPLIED NANO MATERIALS

www.acsanm.org Article

Role of Kinetics and Thermodynamics in Controlling the Crystal Structure of Nickel Nanoparticles Formed on Reduced Graphene Oxide: Implications for Energy Storage and Conversion Applications

Mahmound Tamadoni Saray, Vitaliy Yurkiv, and Reza Shahbazian-Yassar*

Cite This: *ACS Appl. Nano Mater.* 2023, 6, 10033−10043 Read Online

ACCESS | Metrics & More | Article Recommendations | Supporting Information

ABSTRACT: Ultrafast heating has emerged recently to speed up the synthesis processes of nanoparticles and control their morphology. However, it is not clear how the heating rate affects the formation of metal nanoparticles, particularly those formed on substrates. Here, we explored the formation of nickel (Ni) nanoparticles on graphene oxide (GO) substrates under slow (20 °C/min) and ultrafast (10^3 °C/s) heating rates. The experiments were performed in situ on heating microchip devices using an aberration-corrected transmission electron microscope. Interestingly, the GO structure was the most effective in controlling the stability of nanoparticles when ultrafast heating was employed, leading to a hexagonally close-packed Ni phase (*hcp*-Ni) because of less lattice mismatch with the graphitic substrate. On the contrary, *fcc*-Ni nanoparticles formed under a slow heating process where no strong correlation with the GO crystal structure was observed. Additionally, ultrafast heating resulted in smaller-size nanoparticles which could be ascribed to rapid reduction, nucleation rate, and higher diffusion barrier of *hcp*-Ni crystals on rGO. Nevertheless, the stability of the crystal structure of the nickel nanoparticles remains unaffected by their size. These results indicate the crucial role of the substrate on crystal structure during the nonequilibrium processing of materials and the competing effects of thermodynamics versus kinetics in creating novel phases of materials for energy storage and conversion applications.

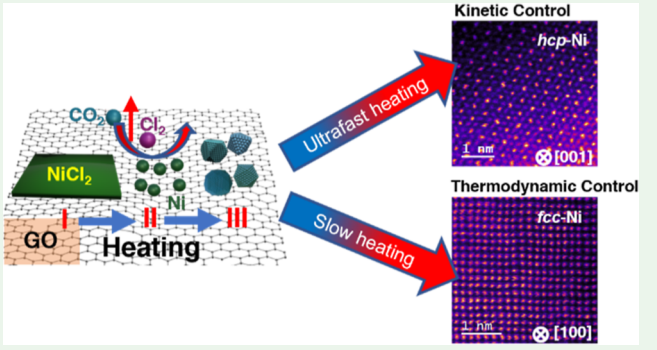

KEYWORDS: *in situ transmission electron microscopy, graphene oxide, nickel nanoparticles, ultrafast heating*

INTRODUCTION

Metal/carbon heterostructures with metal nanoparticles distributed on carbon substrates are employed in various applications such as catalysis,[1,2] nanoelectronics,[3] biosensors,[4] optics,[5] nanobiotechnologies,[6] optoelectronics,[7] and environmental filtering.[8] The characteristics of carbon-supported metal nanostructures are highly influenced by morphology, crystal structure, and distribution of metal nanoparticles and their interactions with carbon supports.[9−12] Among transition metals, Ni nanoparticles have rising interest due to their low cost, fast electron transfer, electroactivity, chemical stability, selectivity, and generic polyvalence merits.[13] For example, Yamada et al.[14] investigated the correlation between Ni crystal structure and photocatalytic hydrogen evolution. They demonstrated that the *hcp*-Ni crystal phase increased the hydrogen evolution rate by more than 400% compared to thermodynamically stable *fcc*-Ni. Recently, Zhang et al.[15] reported outstanding catalytic performance toward hydrogenation of nitrophenols for *hcp*-Ni due to the abundant surface active sites (strong antioxidant ability) than the *fcc*-Ni nanocrystals. Another report by Zhuang et al.[16] demonstrated superior catalytic activity and reusability of *hcp*-Ni NCs in comparison to other nonprecious metal catalysts used in the reduction of 4-nitrophenol by $NaBH_4$. Wang and co-workers investigated the Ni nanoparticles' crystalline phase-dependent oxygen evolution reaction (OER) performance coated with N-doped graphitic carbon layer (Ni@NC) catalysts. They reported that the *hcp*-Ni@NC core−shell nanoparticles demonstrated dramatic enhancement toward the OER compared to *fcc*-Ni@NC. This outstanding performance was attributed to the favorable modulation effect of the *hcp* nickel crystal phase at the core, influencing the electronic state of the outer N-doped carbon shell.[17]

An emerging approach for synthesizing such heterostructures has been the thermal decomposition of metal salts on carbon substrates.[10,18,19] In such cases, it is crucial to carefully

Received: December 25, 2022
Accepted: May 26, 2023
Published: June 9, 2023

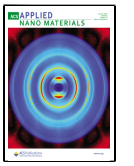

choose heating rates to achieve a thorough reduction of the salt into the metallic state and prevent excessive sintering of the metal nanoparticles throughout the reduction process.[20] Recent interest in nanoparticle synthesis has shifted toward ultrafast heating processes to synthesize new nanomaterials.[10,21−23] For instance, multielement nanoparticles formed on carbon substrates by rapid microwave heating and thermal decomposition of metal salts under an argon atmosphere.[1] Moreover, a rapid thermal shock on defective carbon nanofibers loaded with metal salt resulted in the in situ decomposition of the precursor and the formation of extremely small metallic nanoclusters through nucleation.[24] Yao et al.[22] introduced flash heating (heating rate, ~10^5 K/s) to synthesize single-phase multicomponent nanoparticles. In another work, Yang and co-workers[25] utilized this nonequilibrium synthesis approach to synthesize compositionally homogeneous Cu-based bimetallic alloy nanoparticles despite the inherent immiscibility of the constituent elements.

Despite the vast interest in understanding the behavior of the material under ultrafast heating rates, in situ transmission electron microscopy (TEM) studies exploring the phase stability of materials under such nonequilibrium processes have been scarce.[26] Huang et al.[26] made a significant discovery regarding the formation and stabilization of metallic nanoparticles on amorphous carbon fibers via in situ Joule heating (~10^5 K/s) and slow heating (50 K/s) strategies. Their findings illustrated that contrary to slow heating, ultrafast heating rates yielded stable nanoparticles anchored to graphitic edge defects. Lee et al.[27] conducted in situ scanning transmission electron microscopy (STEM) to observe and analyze the real-time dynamic structural evolution during the formation of MoS_2/graphene heterostructures through the thermolysis of an $(NH_4)_2MoS_4$ precursor at a temperature of 500 °C (heating rate 500 °C/s). They reported precise determination of the atomic structure and dynamic analysis, including edge configuration, formation, and reknitting progress of MoS_2 on graphene.

In this study, we employed in situ heating within aberration-corrected TEM to investigate the crystal structure of Ni nanoparticles on rGO nanosheets via slow and ultrafast heating/cooling approaches. We observed that the ultrafast heating rate resulted in a hexagonal close-packed (*hcp*-Ni) crystal phase. At the same time, thermodynamic factors governed the formation of *fcc*-Ni nanoparticles under slow heating rates.

EXPERIMENTAL SECTION

Sample Preparation. The 10 and 30 mM $NiCl_2{\cdot}6H_2O$/GO suspensions were prepared according to our previous report.[28] The annealing process of the Ni precursor on GO involved heating to 1100 °C and cooling to 25 °C cycles. The initial samples underwent heating with a ramp rate of 10^3 °C/s and 10 °C/min for ultrafast and slow heating experiments, respectively. Once the temperature reached 1100 °C, the samples were subsequently cooled down to room temperature based on their respective heating rates.

TEM Characterization. The experiments involved the investigation of the dynamic microstructure and morphology using in situ TEM at room temperature. The crystal and chemical evaluations were carried out using a JEOL TEM/STEM ARM 200CF equipped with a spherical aberration corrector and a cold field emission gun operated at 200 kV. STEM micrographs were acquired using high-angle annular dark field (HAADF), low-angle annular dark field (LAADF), and annular bright field (ABF) detectors with detector collection angles of 40, 90, and 23 mrad, respectively. STEM imaging was performed with a probe convergence semiangle of 22 mrad using an Orius CCD camera with frame sizes of 512 × 512 pixels. Furthermore, the SAED micrographs of the Ni/GO and Ni/rGO samples were acquired in the TEM diffraction mode with a camera length of 30 cm. For comparative purposes in the in situ heating experiments, a fixed electron diffraction camera length and a selected area aperture were employed. The Digital Micrograph software developed by Gatan Inc was utilized to process the acquired S/TEM images and SAED micrographs. Chemical composition analysis was performed using STEM−energy-dispersive X-ray spectroscopy (EDS) data, which included the elemental spectrum and mappings obtained using an Oxford Xmax 100TLE windowless X-ray detector.

A Gatan imaging filter with a camera length of 20 mm was employed to obtain the electron energy loss spectroscopy (EELS) signal. A probe size of 6C with energy dispersions of 0.3 and 0.75 eV was used, along with an aperture of 2.5 mm and a collection semiangle β of 41.7 mrad. The measurements were conducted on a JEOL 200CF ARM microscope operating at 200 kV, with a beam current of 15.4 pA. After applying power law background subtraction and deconvolution techniques to the core loss spectra, the EELS signal was analyzed and processed using Origin Pro software. To avoid undesired beam-induced effects, the electron beam was intentionally blanked during the thermal treatment experiments.

Density-Functional Theory Methodology. The Vienna ab initio simulation package (VASP) code was utilized to conduct density functional theory (DFT) calculations. The calculations were performed in the generalized-gradient approximation using the Perdew, Burke, and Ernzerhof[29] functional, which accounts for the exchange−correlation energy. For systems with an even number of electrons, nonspin-polarized calculations were conducted, whereas systems with an odd number of electrons underwent unrestricted spin-polarized calculations. In all calculations, a cutoff energy of 450 eV was utilized. Structural optimizations were performed until the forces on atoms reached a magnitude below 0.01 eV/Å. The energy change criterion was set at 0.1 eV. To enhance self-consistent convergence, a Gaussian smearing technique with a width of 0.05 eV was applied. The ab initio molecular dynamics (AIMD) simulations were conducted for a duration of 1000 fs using the canonical ensemble (*NVT*) with a Nosé-Hoover chain thermostat at a temperature of 1100 °C and a time step of 1 fs. The Brillouin zone was sampled using the gamma *k*-point only for AIMD calculations, while 2 × 2 × 1 sampling was employed for the optimization and ground energy calculations of rGO and Ni/rGO.

The nudged elastic band (NEB)[30] technique is used to calculate Ni diffusion over rGO. In the NEB approach, a path connecting two structures is defined by a series of images, or intermediate structures, which represent the transition state. These images are then connected by springs, which are used to nudge the images toward the minimum energy path while maintaining the separation between them. The energy and forces acting on each image are calculated using the VASP, and the NEB algorithm iteratively adjusts the images until the path converges to a minimum energy state. Throughout the NEB calculations, optimization of all images along the diffusion path was carried out simultaneously until the atomic forces in each structure reached a convergence threshold of 0.01 eV/Å. For all calculations, at least a 15 Å vacuum space (distance between the atomic surface and the upper cell boundary) is used. Additionally, to ensure an appropriate representation of the macroscopic rGO structure, different rGO sheets with varying numbers and positions of defects and oxygen groups were calculated to determine the optimal slab thickness. In general, depending upon the system, the ground-state energy value among all considered atomic configurations is negligible. Thus, one representative structure, as shown in Figure S6 is chosen for all calculations. The Atomistic Tool Kit was utilized to construct all atomic structures.[31] Figure S6 illustrates the creation of rGO from a perfect graphite sheet by introducing different defect types and oxygen groups.

https://doi.org/10.1021/acsanm.2c05528
ACS Appl. Nano Mater. 2023, 6, 10033−10043

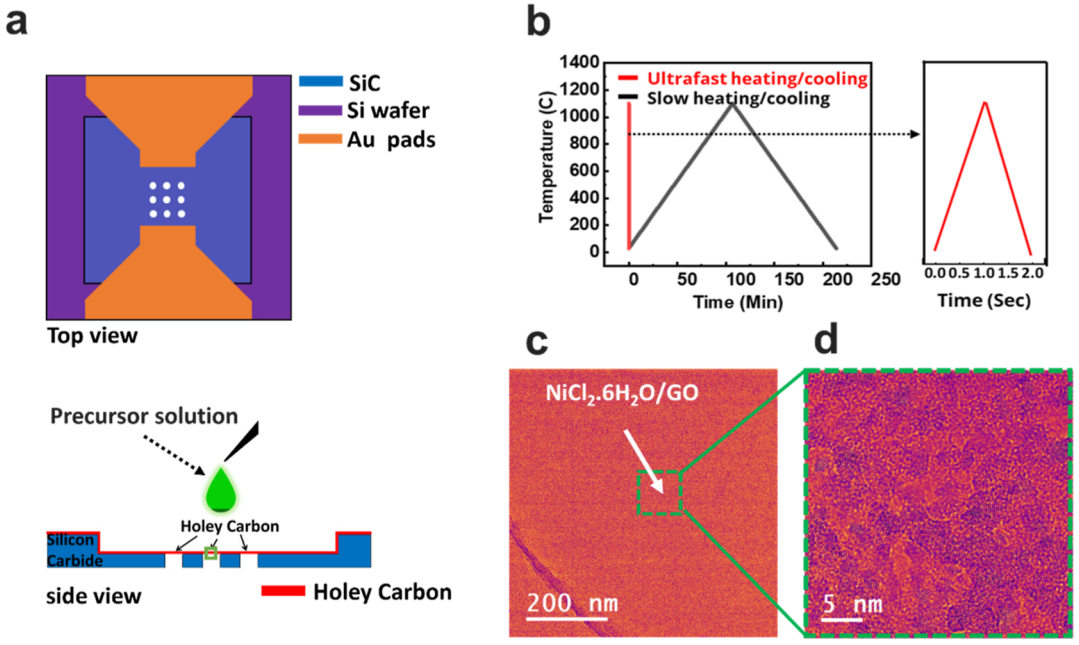

Figure 1. In situ heating experiments for thermal decomposition of the $NiCl_2{\cdot}6H_2O$ precursor on the GO substrate. (a) Schematic illustration of an in situ heating TEM system featuring a microchip heater that allows the investigation of salt precursor decomposition. (b) The graph illustrates the applied heating profiles for both slow and fast heating in situ experiments; the dashed arrow shows the magnified ultrafast heating/cooling profile. (c,d) Low- and high-magnification TEM images of the 10 mM $NiCl_2{\cdot}6H_2O$ salt precursor forming a polycrystalline thin film on GO.

RESULTS AND DISCUSSION

In this study, we conducted in situ TEM investigations involving ultrafast heating/cooling treatments to synthesize polymorph nickel nanoparticles decorated on rGO nanosheets (Ni/rGO). Figure 1 provides a schematic representation of the in situ experimental heating approach employed for the Ni/rGO system. To conduct the experiments, we employed an in situ heating TEM holder equipped with silicon microfabricated chips. The chips utilized in this study consist of a silicon carbide (SiC) heating membrane that includes nine 8 μm holes positioned at the center. These holes are covered with amorphous holey carbon to provide support for the samples. The heating process is initiated by passing an electrical current through the conductive membrane (Figure 1a). The applied heating profiles for the in situ experiments follow heating/cooling rates of 10^3 °C/s and 20 °C/min for ultrafast and slow heating treatments, respectively, as depicted in Figure 1b. The Ni precursor ($NiCl_2{\cdot}6H_2O$) and graphene oxide (GO) suspension was drop-cast on the heating microchip membranes. Subsequently, by applying in situ heating, the $NiCl_2{\cdot}6H_2O$ precursor is expected to thermally decompose into Ni atoms and volatile gas species (Cl_2). Eventually, Ni atoms can form Ni nanoparticles.

Prior to commencing the heating experiments, we used TEM to image the Ni salt layer on the GO substrate. Figure 1c shows a TEM image at low magnification of the 10 mM $NiCl_2{\cdot}6H_2O$/GO mixture located within the holey section of a carbon film, which was supported on a silicon nitride heating microchip. The higher-magnification TEM image in Figure 1d presents a thin layer of polycrystalline nickel chloride hexahydrate nanocrystals with a size of 5−10 nm formed on the GO substrate. Furthermore, the TEM and SAED analyses for the 10 mM and 30 mM $NiCl_2{\cdot}6H_2O$/GO are shown in Figure S1. It can be seen that a thin and more uniform polycrystalline $NiCl_2{\cdot}6H_2O$ layer formed on the GO nanosheets using the 10 mM nickel salt solution compared to the 30 mM nickel salt solution on the GO surface (Figure S1 a, d). Higher-resolution TEM (HR-TEM) characterization of the precursor on GO showed lattice spacings of 5.62 and 5.42 Å corresponding to (001) and (110) planes of the monoclinic $NiCl_2{\cdot}6H_2O$ crystals, respectively (Figure S1b,e). This observation agreed with SAED patterns of the deposited samples, further confirming the formation of the monoclinic crystal structure of $NiCl_2{\cdot}6H_2O$ NPs (space group: $C2/m$) on the GO substrate in both metal salt concentrations after drop-casting onto the heating E-chips (Figure S1c,f). The correlation between our findings and the presence of oxygen functional groups on the surface of GO nanosheets can be observed.

In brief, the formation of a thin layer of polycrystalline nickel chloride nanocrystals on GO might occur through a multistep heterogeneous nucleation process involving the adsorption, coordination, nucleation, and growth of nickel ions on the surface of the GO film. Initially, the mixture of nickel chloride contains nickel ions (Ni^{2+}), chloride ions (Cl^-), and GO nanosheets. These ions can interact with the oxygen functional groups at the surface of GO, such as the carboxylic, epoxide, and hydroxyl groups, through electrostatic interactions and hydrogen bonding.[32] The existence of these functional groups on the surface of GO nanosheets provides them with a robust ability to chemically adsorb metal ions, leading to the formation of metal ion-modified GO films. Therefore, the nickel ions can coordinate with the functional groups on the GO surface, forming coordination complexes.[33−35] The coordination of the nickel ions to the GO surface can occur through the donation of electron pairs from the oxygen atoms of the functional groups to the empty d-orbitals of the nickel ions. As more nickel ions coordinate to the surface of the GO substrate, forming a thin layer or film of the metal salt precursor, they can start to cluster and nucleate, forming small nanocrystals of nickel chloride. These nanocrystals are typically

https://doi.org/10.1021/acsanm.2c05528
ACS Appl. Nano Mater. 2023, 6, 10033−10043

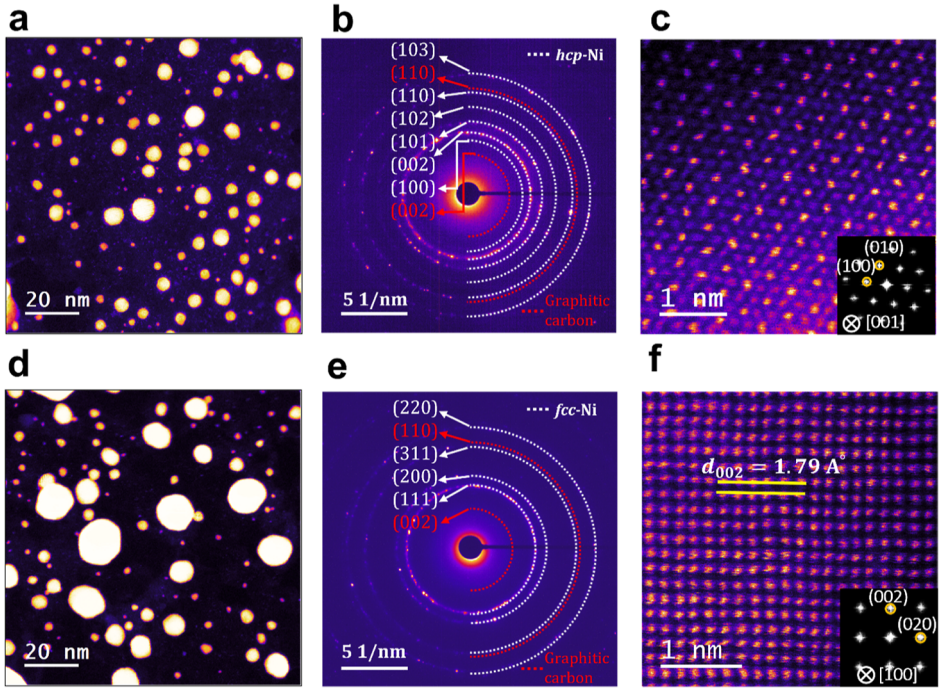

Figure 2. Structure analysis of Ni NPs formed on rGO via (a–c) ultrafast and (d–f) slow heating rates of 10 mM $NiCl_2{\cdot}6H_2O$/GO. (a) HAADF-STEM image at low magnification depicting the Ni NPs distributed on the surface of rGO following an ultrafast heating and cooling cycle. (b) The SAED pattern of Ni/rGO indicates an *hcp* crystal phase of Ni. (c) Atomic-resolution HAADF-STEM image showing an *hcp*-Ni NP crystal on rGO observed from the [001] zone axis perspective. The inset highlights the corresponding FFT of the (100) and (010) planes. (d) The HAADF-STEM image at low magnification depicts the distribution of Ni NPs on rGO following slow heating and cooling treatments. (e) The SAED pattern of Ni/rGO provides evidence for the presence of an *fcc* crystal phase of Ni, along with partial graphitization of GO. (f) The HAADF-STEM image at high resolution depicts a crystal of *fcc*-Ni NPs viewed along the [100] zone axis. The inset emphasizes the corresponding FFT, highlighting the (020) and (002) planes.

between 5 and 10 nm in size and are uniformly distributed on the surface of the GO film. Finally, as the reaction proceeds, the nanocrystals can continue to grow in size by absorbing more nickel ions from the solution and from neighboring nanocrystals on the GO surface. The larger crystalline domains observed for 30 mM $NiCl_2{\cdot}6H_2O$/GO can be explained by the more metal ions available per unit volume in a concentrated metal salt solution. The growth of the nickel salt nanocrystals can be controlled by adjusting the nickel chloride precursor's reaction time, temperature, and concentration, as shown in Figures 1C and S1.

We initially explored the ultrafast heating rate effect on the Ni nanoparticles formed on the GO substrate. The false-colored LAADF-STEM image in Figure 2a illustrates that heating the precursor salt (10 mM $NiCl_2{\cdot}6H_2O$/GO) yielded an exemplary distribution of Ni NPs on rGO nanosheets. A representative SAED pattern of a large-scale area of multiple nanoparticles after ultrafast heating synthesis is presented in Figure 2b. The SAED micrograph features bright spots from large particles and diffraction rings of numerous tiny Ni nanocrystalline reflections. The electron diffraction with six diffraction rings depicts a polycrystalline nature matching the metastable hexagonally close-packed Ni phase (*hcp*-Ni). The spacings of diffraction rings are consistently indexed based on the hexagonal metallic Ni (space group, $P6_3/mmc$, a = 2.622, c = 4.321) structure. We should emphasize that no diffractions related to *fcc*-Ni or Ni oxide Bragg peaks in the SAED pattern were observed, confirming pure *hcp*-Ni nanoparticles' formation upon ultrafast heating treatment. Additionally, ultrafast heating of the concentrated metal salt precursor (30 mM $NiCl_2{\cdot}6H_2O$/GO) resulted in the formation of larger and more condensed nanoparticles with the *hcp*-Ni phase (Figure S2a,c). *hcp*-Ni is a thermodynamically metastable phase, and its formation requires particular circumstances. Additionally, the innermost ring highlighted with a red semicircle in the SAED pattern (002) corresponds to the formation of graphitic carbon domains with an averaged d-spacing of 3.46 Å upon high-temperature heating treatment. Furthermore, the atomic-resolution HAADF-STEM image of an individual Ni particle is shown in Figure 2c. The corresponding fast Fourier transform (FFT) pattern in the inset is consistent with metastable *hcp*-Ni projected in the [001] direction. More atomic structural information, including HAADF and ABF-STEM images of another Ni NP corroborating hexagonal phase formation during the high-temperature ultrafast heating process, is provided in Figure S3. The atomic resolution HAADF-STEM image of the NP and corresponding FFT coincide with the [012] zone axis of *hcp*-Ni (Figure S3a). Furthermore, the interplanar spacing of 2.27 Å corresponds to the (100) lattice plane highlighted in the inverse FFT (IFFT) image (Figure S3b). Also, the atomic model of *hcp*-Ni at the [012] zone axis well matches the experimental observation illustrated in the ABF-STEM image (Figure S3c). It is worth mentioning that we did not observe any light elements, including carbon or oxygen, in the ABF-STEM image, which further confirmed that the Ni crystal is a pure *hcp*-Ni phase. However, upon undergoing the slow heating treatment, the rGO substrate exhibits the decoration of cubic-phase nickel nanoparticles (Figure 2d). The electron diffraction micrograph was obtained from the nanoparticles attached to the rGO

https://doi.org/10.1021/acsanm.2c05528
ACS Appl. Nano Mater. 2023, 6, 10033–10043

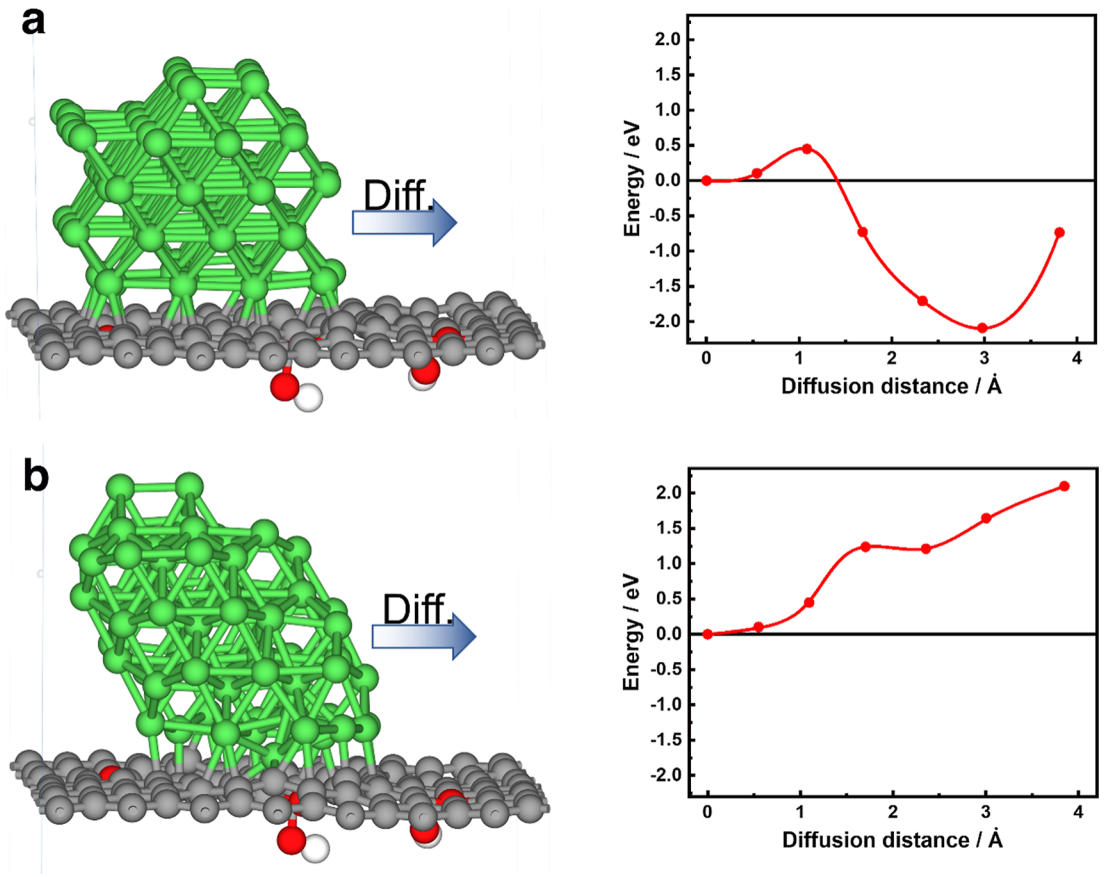

Figure 3. (a) DFT calculation results of *fcc* (a) and *hcp* (b) Ni diffusion over the rGO surface. Pictures on the left illustrate the atomic structure of *fcc*- and *hcp*-Ni, while pictures on the right show energetics of the corresponding diffusion. The illustration depicts carbon, oxygen, hydrogen, and nickel atoms in gray, red, white, and green spheres, respectively.

surface. Figure 2e displays clearly defined diffraction rings in good agreement with the (111), (200), (220), and (311) crystallographic planes of the thermodynamically stable face-centered cubic Ni (*fcc*-Ni, space group: $Fm\bar{3}m$) phase. Additionally, in Figure 2f, the HAADF-STEM image at atomic resolution displays a Ni nanocrystal, clearly demonstrating its single-crystalline structure. The image reveals a discernible lattice spacing of 1.79 Å (indicated by yellow lines), which corresponds to the (200) planes of the *fcc*-Ni structure. Furthermore, slow heating of the concentrated metal salt precursor (30 mM $NiCl_2{\cdot}6H_2O$/GO) led to the formation of larger and variable-size nanoparticles with the *fcc*-Ni phase (Figure S2b,d). Additionally, similar to our earlier work,[28] the GO substrate partially crystallized into graphitic carbon (g-C) upon the heating process, as evidenced via the centered red semicircle ring in the SAED patterns corresponding to the (002) and (110) plane of graphitic carbon.

We should also mention that the rapid heating/cooling approach resulted in smaller and more uniform-size Ni NPs formed on rGO than the slow heating process. Figure S4 displays the particle size distribution of Ni nanoparticles formed on rGO via ultrafast and slow heating for different concentrations of $NiCl_2{\cdot}6H_2O$/GO. The Ni NPs with an overall average diameter size and dispersions of 3.61 ± 1.52 and 5.56 ± 2.02 nm formed by the fast rate of heating/cooling of 10 and 30 mM $NiCl_2{\cdot}6H_2O$ on rGO, respectively. However, by subjecting the deposited 10 and 30 mM $NiCl_2{\cdot}6H_2O$/GO samples to slow heating and subsequent cooling, Ni NPs were formed with average sizes of 5.66 ± 3.38 and 9.81 ± 5.84 nm, respectively. This observation is likely related to the difference in the kinetics of nucleation and growth of the NPs. In the rapid heating/cooling approach, short duration rapidly heats the metal precursor and rGO substrate. Rapid heating leads to a more intense and homogeneous distribution of the nuclei on the GO substrate surface, which promotes the formation of smaller and more uniformly sized NPs. The cooling step following the heating also occurs quickly, which limits the diffusion and coalescence of the NPs, leading to a more uniform size distribution. In contrast, the slow heating process may lead to more prolonged exposure to high temperatures, which can form larger and less uniform NPs due to the higher likelihood of coalescence and Ostwald ripening.

In order to better understand the influence of *fcc*-Ni vs *hcp*-Ni formation over rGO, the DFT calculations have been performed. We studied the stability and the favorable pathways of Ni (*fcc* vs *hcp*) diffusion over rGO. Several rGO monolayers starting from a perfect graphite sheet with varying defects, oxygen, and hydroxyl groups position have been created and optimized (cf. Figure S6). It is found that all such structures exhibit comparable ground-state energy as long as the number of defects and oxygen-containing groups remains constant, which is consistent with the prior literature.[36,37] Thus, one representative rGO configuration with single and double defect types was chosen for the DFT calculations. The *fcc*-Ni and *hcp*-Ni atomic structures were optimized, and Ni diffusion over rGO was studied. Figure 3 shows the DFT calculation results of Ni (*fcc* and *hcp*) diffusion over rGO. In Figure 3, the left-hand images illustrate the atomic structures, while the right-

https://doi.org/10.1021/acsanm.2c05528
ACS Appl. Nano Mater. 2023, 6, 10033−10043

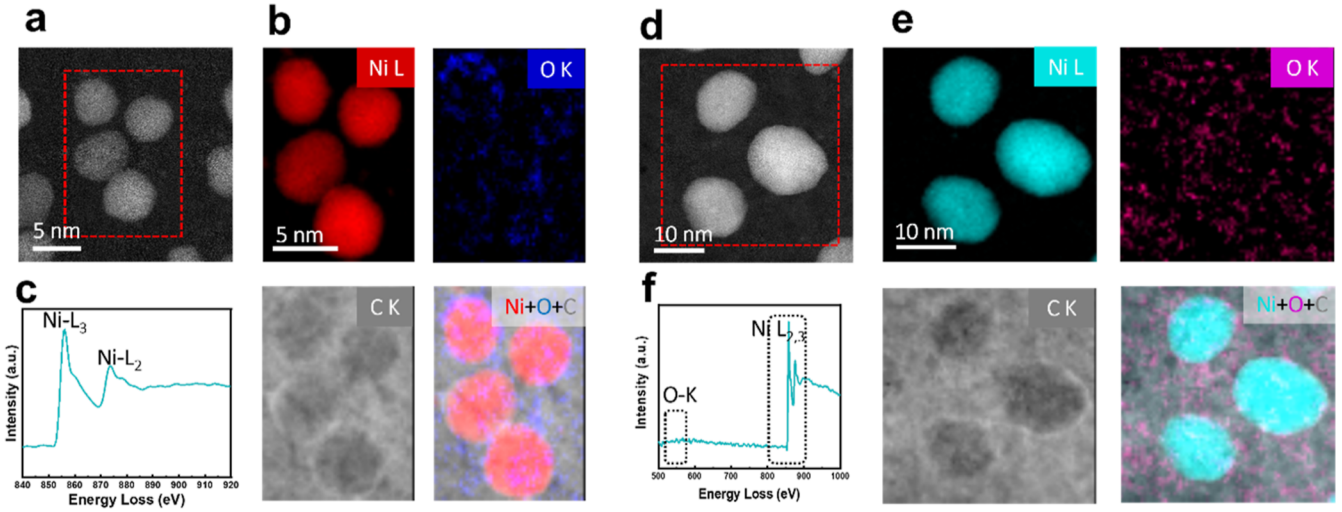

Figure 4. STEM-EELS characterization on the chemical composition of Ni NPs synthesized on rGO. (a) LAADF-STEM image of two Ni NPs on rGO formed by ultrafast heating. (b) EELS maps extracted from the Ni L-edge, O K-edge, C−K, and the RGB. (c) ELNES of the Ni $L_{2,3}$-edge obtained from an individual Ni nanoparticle. (d) LAADF-STEM image of Ni NPs on rGO produced via the slow heating approach. (e) EELS maps extracted from the Ni L-edge, O K-edge, C−K, and the RGB image. (f) EEL spectrum extracted from the red box region in (d).

hand images display the energetics associated with the diffusion of nickel Ni. However, the DFT calculations reveal that the diffusion of *fcc*-Ni exhibits an energetic advantage of 0.73 eV, accompanied by an activation barrier of 0.45 eV. Interestingly, there is a more energetically beneficial adsorption configuration with an energy of −2.08 eV compared to the initial state detected in the NEB calculations. This adsorption corresponds to the position over a single defective side. Nevertheless, DFT calculation results indicate that *fcc*-Ni diffusion over rGO is a relatively favorable process. Contrarily, the diffusion of *hcp*-Ni over the same rGO sheet is significantly less favorable, as revealed by the DFT calculations in Figure 3b. Specifically, the same diffusion distance of 3.9 Å by *hcp*-Ni is supported by an energy increase of 2.1 eV with an intermediate barrier at 1.7 Å. Such a drastic difference between *fcc*- and *hcp*-Ni diffusion is attributed to the stronger adsorption between the adjacent *hcp*-Ni layer and rGO, as obtained in the DFT calculations. Due to the structural differences between the *fcc* and *hcp* configurations, the last layer of the Ni slab facing toward the rGO has a different number of bonds with C atoms, leading to significantly different adsorption energy. This can be observed in Figure 3b, where one of the Ni atoms was pulled toward rGO, making the diffusion process less favorable. It was further proven that *hcp*-Ni is more tightly adsorbed to rGO by calculating the energy of desorption. In particular, to desorb *fcc*-Ni from rGO, 7.5 eV is needed, as illustrated in Figure S7a. For the same process, 9 eV is required for *hcp*-Ni (cf. Figure S7b). Although both processes are practically impossible considering very high adhesion energy, *fcc*-Ni is still slightly less energetically demanding compared to *hcp*-Ni.

To gain further insights into the experimentally observed phenomena, we conducted DFT and AIMD simulations to investigate the behavior of Ni on the surface of rGO. The AIMD simulations for 1000 fs at 1100 °C in the presence of 16 Ni atoms over rGO were performed. This temperature corresponds to the maximum temperature point in our experimental measurements (Figure 1). The AIMD simulation results (Figure S8) show a significant Ni atom movement over the rGO surface. This could be expected for such a high temperature. However, we have further observed *fcc*-Ni formation at the end of AIMD calculations (last image in Figure S8). A typical Ni *fcc* structure starts to form in the middle with an identical bond length as in the *fcc*-Ni slab. This indicates that slow thermodynamically controlled heating should lead to *fcc*-Ni formation. At the same time, rapid point temperature increase should produce *hcp*-Ni to overcome a significant activation barrier, as obtained in the DFT calculations. Moreover, as the DFT calculations showed a higher energy barrier for the *hcp*-Ni NP diffusion on the GO substrate than *fcc*-Ni NPs, this may also contribute to the smaller size of the *hcp*-Ni NP formation upon ultrafast heating.

We should emphasize that chemical analysis is necessary to distinguish the correct type of crystals because of the crystal similarity between *hcp*-Ni and *hcp*-Ni_3C (resulting in a similar diffraction pattern). To validate the chemical composition of the synthesized Ni NPs on rGO) nanosheets, STEM-EELS was employed. LAADF-STEM enables better image contrast visualization for light elements like carbon, as shown in Figure 4a. STEM-EELS on the Ni/rGO hybrid composite was performed via ultrafast heating of 10 mM $NiCl_2{\cdot}6H_2O$/GO collected from the red dashed box region encompassing four nanoparticles, as shown in Figure 4a. Accordingly, the elemental surface distribution checked by EELS maps from the corresponding region of interest (ROI) is presented in Figure 4b. The homogeneous Ni element distribution map without oxygen in the corresponding particles confirmed pure metallic Ni NP formation on the rGO surface upon ultrafast heating treatment. A very weak O−K signal in the synthesized Ni/rGO composite comes from the rGO support surface. The EEL spectrum extracted from ROI represents the pure metallic Ni NP formation upon fast heating treatment (Figure 4c). Our observation is consistent with the reported thermal reduction of GO via in situ TEM/EELS, which featured almost total removal of oxygen functional groups and graphitization at 1200 °C.[38]

In addition, the STEM-EELS analyses of the NPs formed on rGO after slow heating of 10 mM $NiCl_2{\cdot}6H_2O$/GO are also provided. Figure 4d,e shows the LAADF-STEM image of three particles and corresponding EELS maps of oxygen, nickel, and

https://doi.org/10.1021/acsanm.2c05528
ACS Appl. Nano Mater. 2023, 6, 10033−10043

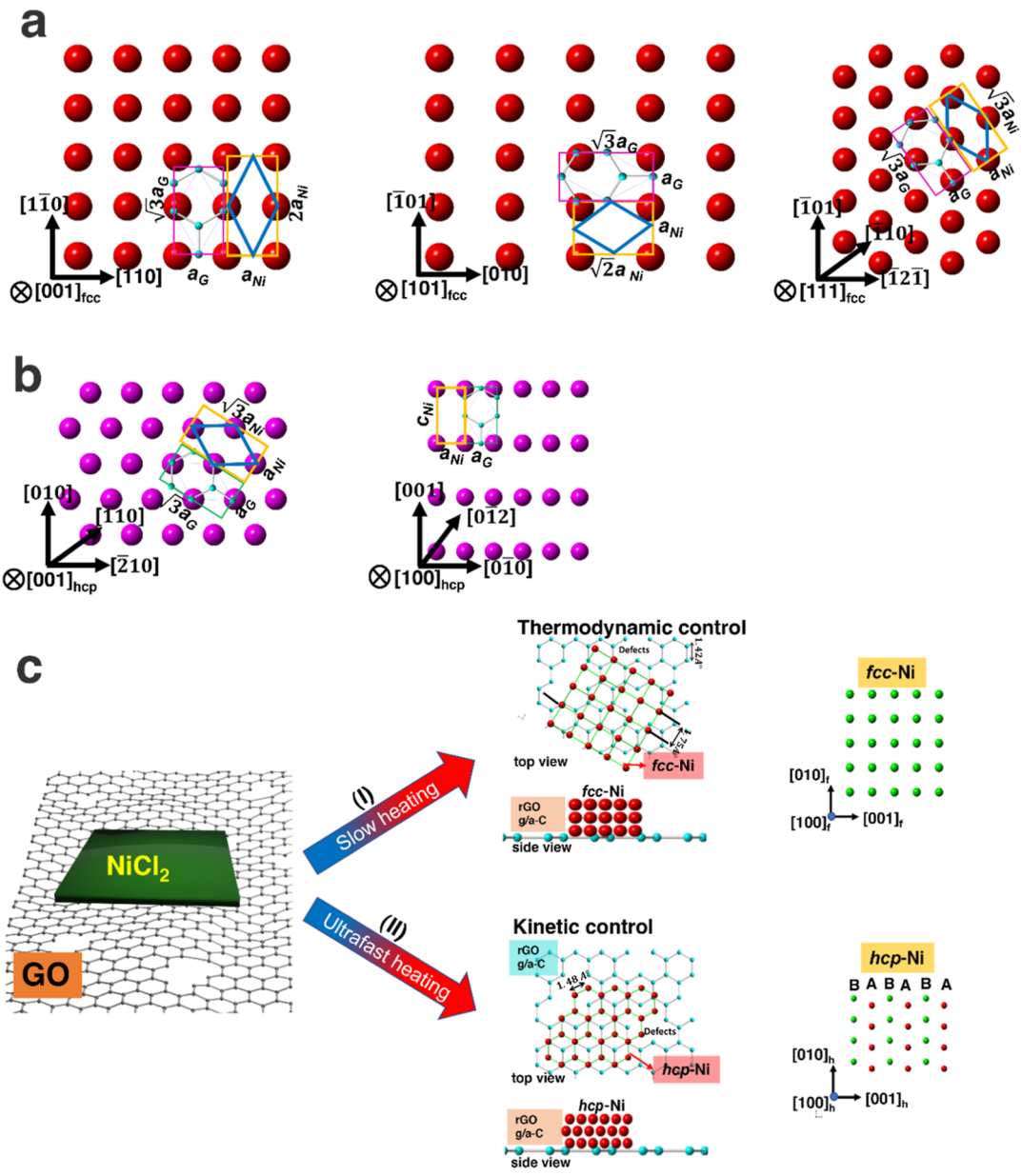

Figure 5. (a) Illustration of the graphene unit cell and crystallographic orientations of Ni NPs synthesized on rGO via ultrafast and slow heating rates. (a) Comparison of the graphene lattice and *fcc*-Ni (001), (101), and (111) planes. (b) Comparison of the graphene lattice and *hcp*-Ni (001) and (100) planes. (c) Schematic of crystal structures adopted by Ni NPs upon slow and ultrafast thermolysis of $NiCl_2$ on GO nanosheets. (a) Stepwise transformation process of the $NiCl_2$ precursor into Ni nanoparticles through thermal decomposition can be described as follows: I: initially, a solid film of the $NiCl_2{\cdot}6H_2O$ precursor forms on the GO substrate. II: As the heating process takes place, the precursor salt and GO undergo a transformation, resulting in the formation of Ni atoms along with the release of gaseous byproducts. III: Finally, the Ni atoms further aggregate to form Ni nanoparticles. (b) In slow heating, the thermodynamically stable *fcc*-Ni crystal phase forms on rGO. The representative crystal structure is shown at the [100] zone axis. (b) Upon ultrafast heating, the *hcp*-Ni phase forms on rGO. The corresponding crystal with the "ABAB" stacking model is shown at the [100] zone axis.

overlaid RGB from the red box region, respectively. It clearly confirms the pure Ni phase composition for the NPs. The core loss EEL spectrum extracted from the corresponding ROI (Figure 4f) includes the Ni L-edge white line with no sign of O−K-edge presence, suggesting that the thin oxygen coverage in Figure 4e is due to the rGO substrate. It is clear that the spectrum from the ROI proved a dominant Ni sharp white line with no prominent oxygen peak, excluding the possibility of the oxide nature of the formed Ni NP. Through the analysis of the energy loss near-edge fine structure (ELNES) of the Ni NP depicted in Figure 4f, it was verified that the intensity ratio of the Ni L_3/L_2 white lines corresponded to the zero-valence oxidation state of the nickel element.[39,40] We should emphasize that the L_3/L_2 white line intensity ratio is a reliable measure for determining the oxidation state of transition metals due to its direct correlation with 3d orbital occupancy.[40] Additionally, our STEM-EDS analysis on the resultant nickel nanoparticles further demonstrates no discernible oxygen peak (Figure S5), which agrees with EELS results, confirming the formation of pure Ni NPs under the thermal decomposition of metal salts on the GO substrate.

https://doi.org/10.1021/acsanm.2c05528
ACS Appl. Nano Mater. 2023, 6, 10033−10043

Overall, our chemical analysis ruled out the possibility of *hcp*-Ni_3C formation or the presence of nickel oxide compounds. It has been observed that carbide formation can occur when carbon materials are heated in the presence of catalytic active metals like nickel.[41,42] At elevated temperatures, it has been discovered that carbide compounds can undergo instability and decompose, resulting in the formation of graphite and metals.[43,44] In our experimental setup, where the temperature exceeds the thermal decomposition threshold of Ni-carbide (~500 °C), no transitional Ni-carbide was detected.[42]

Identifying new crystal phases presents an opportunity to explore novel functionalities attributed to the distinctive atomic arrangements and electronic structures exhibited by these polymorphs. Therefore, the relationship between the size of Ni NPs, their crystal structure, and the GO effect is worthy of further discussion. The energy discrepancy per atom in bulk between the *fcc* and *hcp* phases of nickel, denoted as $\Delta E_B(fcc-hcp)$, is relatively minor at −28 meV/atom. This suggests that the *fcc* crystal structure is more energetically preferred under normal ambient conditions.[45,46] *hcp*-Ni can become stable under certain conditions.

Our study does not show size scale dependency on the crystal structure of the Ni NPs. Our work observed hexagonal (3.61 ± 1.52 and 5.56 ± 2.02 nm) and cubic nickel (5.66 ± 3.38 and 9.81 ± 5.84 nm)-phase nanoparticles from the10 mM and 30 mM $NiCl_2{\cdot}6H_2O$/GO mixture, formed on the rGO substrate, respectively. For instance, the large nanoparticle (>10 nm diameter) demonstrates the *hcp*-Ni phase. Our observation contrasts with the previous reports demonstrating the tendency to stabilize *hcp*-Ni nanocrystals over *fcc*-Ni below the critical size limit of ~5 nm due to the lower surface energy of the hexagonal structure.[47,48] This is argued from the point of view that smaller-size nanoparticles are likely to be affected by surface energy contributions to the overall energy of nanoparticles. Therefore, the higher surface-to-volume ratio of nanoscale materials can affect the total Gibbs free energy, leading to the formation and stabilization of new phases, including metastable nanocrystal structures.[49]

The presence of *hcp*-Ni NPs on rGO nanosheets, despite the absence of a size dependency on the Ni crystal structure, can be ascribed to the influence of the carbon substrate. Considering the lack of Ni crystal structure-size dependency, the observation of *hcp*-Ni NPs on rGO nanosheets can be explained by considering the role of the carbon substrate. We investigated the mismatches in lattice structures among the graphene unit cell, *fcc*-Ni, and *hcp*-Ni crystal phases for various crystallographic orientations, as illustrated in Figure 5a,b. In order to maintain consistent comparisons of lattice mismatches between different Ni crystallographic orientations and the graphene unit cell, a rectangular repeating cell was employed, regardless of their respective unit cell shapes. Since the base axis of the Ni repeating unit and graphene unit cell are close, the calculation of lattice mismatches involved a comparison of the vertical axes exclusively. It is reported that the lattice constant for graphite lattice (a_G) is 2.461.[50] The calculated lattice mismatches between graphene and (111), (110), and (001) planes of *fcc*-Ni are 1.4, −17.4, and 16.8%, respectively (Supporting Information Note 1). In comparison, the mismatch between graphene and (001) and (100) planes of *hcp*-Ni is calculated to be 7.7 and 1.9%, respectively (Note S1). Overall, nickel with a hexagonal phase has a well-matched interface with the graphene substrate. An additional factor can be the lower surface energy of *hcp*-Ni compared to *fcc*-Ni. Lin et al.[46] conducted calculations to determine the surface energies (γ_i) of *fcc* and *hcp*-Ni. Their findings reveal that the surface energies of the low-index facets, specifically Ni(001)hcp and Ni(111)fcc, are 115 and 121 meV/Å^{-2}, respectively. Moreover, the total surface energy of *hcp*-Ni is 122 meV/Å^2, which is slightly lower by 3 meV/Å^2 compared to the surface energy of *fcc*-Ni. Furthermore, because of the brief duration of exposure to high temperatures followed by rapid cooling, the formed *hcp*-Ni could not afford atomic interdiffusion and reordering (configurational rearrangements) into thermodynamic equilibrium. Therefore, the Ni atom arrangement follows the *hcp* configuration that is the closest match to the rGO crystal structure. However, nickel nuclei form with adequate time for high interdiffusion and structural relaxation in slow heating to adopt thermodynamically favored *fcc*-Ni crystal formation on rGO.

Furthermore, ultrafast heating should result in quick Ni precursor decomposition and high reduction burst (decomposition rate) of Ni cations to Ni atoms and formation of smaller Ni NPs.[51−53] In addition, the presence of defects on GO and their anchoring effect[26,54] should further limit the diffusion of Ni atoms at short time spans for ultrafast heating. The molecular dynamics simulations reveal that these surface defects serve as anchor points, effectively stabilizing the nanoparticles and considerably slowing down their diffusion and coalescence on the rGO surface.[55,56]

General overview of the proposed stable metastable *fcc*-Ni and *hcp*-Ni morph formation during the slow and ultrafast heating of $NiCl_2{\cdot}6H_2O$ on the GO substrate illustrated in Figure 5. In brief, during the slow heating (Figure 5c, (I)), the prolonged exposure at elevated temperature favors the formation of thermodynamically stable *fcc* nickel. The atomic model of Ni NPs with the *fcc* crystal structure is shown in the inset. In contrast, upon ultrafast heating, Ni atoms anchored to functional groups and defects on the GO surface adopt the *hcp* crystal structure that minimized the lattice mismatch with rGO. Furthermore, the subsequent ultrafast cooling freezes the formed hexagonal nickel phase, making them stable at room temperatures. The *hcp* crystal structure phase of Ni NPs with "ABAB" stacking is depicted in the inset (Figure 5c, (II)).

From a general point of view, synthesizing nanoparticles via an alternative ultrafast approach, such as laser-induced heating, also could provide insights into the ultrafast decomposition of metal precursors at higher temperatures, transformation, and restructuring in the nanosecond timescale, which deserves future studies.[57,58] Furthermore, the findings of this study could be applied to a better understanding of Ni/rGO nanocomposites' significant technological impacts in several relevant fields, including (I) heterogeneous catalyzes such as hydrogenation, oxidation, and reduction.[59−61] The high surface area-modified electronic properties and abundant active sites of the nanocomposites facilitate the adsorption of reactant molecules and enhance the catalytic activity and (II) energy storage like lithium-ion batteries and supercapacitors. Incorporating Ni nanoparticles into the rGO matrix improves the electron conductivity and stabilizes the electrode structure, leading to better electrochemical performance.[62−64]

CONCLUSIONS

In summary, using in situ TEM, we explored the crystal structure of Ni nanoparticles formed on GO substrates during ultrafast and slow heating/cooling of $NiCl_2{\cdot}6H_2O$ salt. Our

https://doi.org/10.1021/acsanm.2c05528
ACS Appl. Nano Mater. 2023, 6, 10033−10043

finding indicates that slow heating/cooling treatment results in a thermodynamically stable *fcc*-Ni phase. On the other hand, under ultrafast heating rate conditions, the Ni phase adopted the hexagonal crystal structure on rGO due to less lattice mismatch with the graphitic substrate. Additionally, *hcp*-Ni NPs show a smaller average size than the *fcc*-Ni counterpart because of the limited diffusion on GO and the high nucleation rate during the ultrafast heating process. Our study demonstrates the importance of the heating rate and carbon substrate in stabilizing metastable forms of materials as new metal-carbon heterostructures for energy storage and conversion applications.

■ ASSOCIATED CONTENT

Supporting Information

The Supporting Information is available free of charge at https://pubs.acs.org/doi/10.1021/acsanm.2c05528.

TEM images and SAED patterns of the Ni precursor on GO with different concentrations, HAADF-STEM images and SAED patterns of Ni NPs/rGO hybrid, atomic resolution STEM images of an *hcp*-Ni nanoparticle, size distribution of Ni nanoparticles, EDS compositional data of Ni/rGO synthesized under ultrafast and slow heating conditions, structures for the ab initio calculations, DFT calculation results of *fcc*-Ni and *hcp*-Ni desorption from the rGO substrate, and lattice mismatch percentage calculations between graphene and *fcc* and *hcp* nickel phases at different crystallographic orientations (PDF)

■ AUTHOR INFORMATION

Corresponding Author

Reza Shahbazian-Yassar − *Department of Mechanical and Industrial Engineering, University of Illinois Chicago (UIC), Chicago, Illinois 60607, United States;* orcid.org/0000-0002-7744-4780; Email: rsyassar@uic.edu

Authors

Mahmound Tamadoni Saray − *Department of Mechanical and Industrial Engineering, University of Illinois Chicago (UIC), Chicago, Illinois 60607, United States*

Vitaliy Yurkiv − *Department of Aerospace and Mechanical Engineering, University of Arizona, Tucson, Arizona 85721, United States*

Complete contact information is available at: https://pubs.acs.org/10.1021/acsanm.2c05528

Author Contributions

M.T.S. performed thermal experiments and characterizations. M.T.S. wrote the manuscript. V.Y. performed DFT and AIMD simulations. R.S.Y. conceptualized and supervised the project. All authors contributed to the discussion and manuscript preparation.

Notes

The authors declare no competing financial interest.

■ ACKNOWLEDGMENTS

R.S.Y. is thankful to the National Science Foundation (NSF) for award number DMR-1809439. The present work made use of the JEOL JEM-ARM200CF in the Electron Microscopy Service of the Research Resources Center, RRC, at the University of Illinois Chicago (UIC). V.Y. acknowledges the computational support by the University of Arizona High Performance Computing (HPC) facility, as well as the financial support from NSF award number DMR-2311104.

■ ABBREVIATIONS

GO, graphene oxide
Ni, nickel
TEM, transmission electron microscopy
STEM, scanning transmission electron microscopy
EDS, energy-dispersive X-ray spectroscopy
HAADF, high-angle annular dark field
LAADF, low-angle annular dark field
EELS, electron energy loss spectroscopy
SAED, selected area electron diffraction
DFT, density functional theory
VASP, Vienna ab initio simulation package
AIMD, ab initio molecular dynamics
NEB, nudged elastic band

■ REFERENCES

(1) Qiao, H.; Saray, M. T.; Wang, X.; Xu, S.; Chen, G.; Huang, Z.; Chen, C.; Zhong, G.; Dong, Q.; Hong, M.; Xie, H.; Shahbazian-yassar, R.; Hu, L. Scalable Synthesis of High Entropy Alloy Nanoparticles by Microwave Heating. *ACS Nano* **2021**, *15*, 14928−14937.

(2) Fan, Z.; Zhang, H. Template Synthesis of Noble Metal Nanocrystals with Unusual Crystal Structures and Their Catalytic Applications. *Acc. Chem. Res.* **2016**, *49*, 2841−2850.

(3) Artiles, M. S.; Rout, C. S.; Fisher, T. S. Graphene-Based Hybrid Materials and Devices for Biosensing. *Adv. Drug Delivery Rev.* **2011**, *63*, 1352−1360.

(4) Husain, Q. Biosensor Applications of Graphene-Nanocomposites Bound Oxidoreductive and Hydrolytic Enzymes. *Anal. Methods* **2017**, *9*, 6734−6746.

(5) Cai, S.; Zheng, C.; Xiao, X.; Li, W.; Chen, W. Graphene-Based Hierarchical Sandwich-Type Hybrid Nanostructures for Optical Limiters. *Opt. Mater.* **2019**, *98*, 109453.

(6) Nguyen, K. T.; Zhao, Y. Integrated Graphene/Nanoparticle Hybrids for Biological and Electronic Applications. *Nanoscale* **2014**, *6*, 6245−6266.

(7) Zheng, Z.; Zu, X.; Zhang, Y.; Zhou, W. Rational Design of Type-II Nano-Heterojunctions for Nanoscale Optoelectronics. *Mater. Today Phys.* **2020**, *15*, 100262.

(8) Tang, K.; Hong, T. Z. X.; You, L.; Zhou, K. Carbon-Metal Compound Composite Electrodes for Capacitive Deionization: Synthesis, Development and Applications. *J. Mater. Chem. A* **2019**, *7*, 26693−26743.

(9) Ruffino, F.; Giannazzo, F. A Review on Metal Nanoparticles Nucleation and Growth on/in Graphene. *Crystals* **2017**, *7*, 219.

(10) Lai, L.; Li, J.; Deng, Y.; Yu, Z.; Wei, L.; Chen, Y. Carbon and Carbon/Metal Hybrid Structures Enabled by Ultrafast Heating Methods. *Small Struct.* **2022**, *3*, 2200112.

(11) Rumptz, J. R.; Zhao, K.; Mayo, J.; Campbell, C. T. Size-Dependent Energy of Ni Nanoparticles on Graphene Films on Ni (111) and Adhesion Energetics by Adsorption Calorimetry. *ACS Catal.* **2022**, *12*, 12632−12642.

(12) Campbell, C. T.; Mao, Z. Chemical Potential of Metal Atoms in Supported Nanoparticles: Dependence upon Particle Size and Support. *ACS Catal.* **2017**, *7*, 8460−8466.

(13) Oshchepkov, A. G.; Braesch, G.; Bonnefont, A.; Savinova, E. R.; Chatenet, M. Recent Advances in the Understanding of Nickel-Based Catalysts for the Oxidation of Hydrogen-Containing Fuels in Alkaline Media. *ACS Catal.* **2020**, *10*, 7043−7068.

(14) Yamada, Y.; Miyahigashi, T.; Kotani, H.; Ohkubo, K.; Fukuzumi, S. Photocatalytic Hydrogen Evolution with Ni Nanoparticles by Using 2-Phenyl-4-(1-Naphthyl)Quinolinium Ion as a Photocatalyst. *Energy Environ. Sci.* **2012**, *5*, 6111.

(15) Zhang, C.; Yang, J.; Liu, Y.; Li, Y.; Dai, Z.; Han, M.; Bao, J. Catalytic Hydrogenation of Nitrophenols by Cubic and Hexagonal Phase Unsupported Ni Nanocrystals. *ChemistrySelect* **2019**, *4*, 42−48.
(16) Zhuang, J.; Liu, X.; Ji, Y.; Gu, F.; Xu, J.; Han, Y.; Xu, G.; Zhong, Z.; Su, F. Phase-Controlled Synthesis of Ni Nanocrystals with High Catalytic Activity in 4-Nitrophenol Reduction. *J. Mater. Chem. A* **2020**, *8*, 22143−22154.
(17) Wang, C.; Wang, Y.; Yang, H.; Zhang, Y.; Zhao, H.; Wang, Q. Revealing the Role of Electrocatalyst Crystal Structure on Oxygen Evolution Reaction with Nickel as an Example. *Small* **2018**, *14*, 1802895.
(18) Yin, Y.; Alivisatos, A. P. Colloidal Nanocrystal Synthesis and the Organic−Inorganic Interface. *Nature* **2005**, *437*, 664−670.
(19) Uflyand, I. E.; Dzhardimalieva, G. I. *Nanomaterials Preparation by Thermolysis of Metal Chelates*; Springer Series on Polymer and Composite Materials; Springer Cham, 2018.
(20) Newkirk, A. E.; McKee, D. W. Thermal Decomposition of Rhodium, Iridium, and Ruthenium Chlorides. *J. Catal.* **1968**, *11*, 370−377.
(21) Dou, S.; Xu, J.; Cui, X.; Liu, W.; Zhang, Z.; Deng, Y.; Hu, W.; Chen, Y. High-Temperature Shock Enabled Nanomanufacturing for Energy-Related Applications. *Adv. Energy Mater.* **2020**, *10*, 2001331.
(22) Yao, Y.; Huang, Z.; Xie, P.; Lacey, S. D.; Jacob, R. J.; Xie, H.; Chen, F.; Nie, A.; Pu, T.; Rehwoldt, M.; Yu, D.; Zachariah, M. R.; Wang, C.; Shahbazian-Yassar, R.; Li, J.; Hu, L. Carbothermal Shock Synthesis of High-Entropy-Alloy Nanoparticles. *Science* **2018**, *359*, 1489−1494.
(23) Jiang, R.; Da, Y.; Han, X.; Chen, Y.; Deng, Y.; Hu, W. Ultrafast Synthesis for Functional Nanomaterials. *Cell Rep. Phys. Sci.* **2021**, *2*, 100302.
(24) Yao, Y.; Huang, Z.; Xie, P.; Li, T.; Lacey, S. D.; Jiao, M.; Xie, H.; Fu, K. K.; Jacob, R. J.; Kline, D. J.; Yang, Y.; Zachariah, M. R.; Wang, C.; Shahbazian-Yassar, R.; Hu, L. Ultrafast, Controllable Synthesis of Sub-Nano Metallic Clusters through Defect Engineering. *ACS Appl. Mater. Interfaces* **2019**, *11*, 29773−29779.
(25) Yang, C.; Ko, B. H.; Hwang, S.; Liu, Z.; Yao, Y.; Luc, W.; Cui, M.; Malkani, A. S.; Li, T.; Wang, X.; Dai, J.; Xu, B.; Wang, G.; Su, D.; Jiao, F.; Hu, L. Overcoming Immiscibility toward Bimetallic Catalyst Library. *Sci. Adv.* **2020**, *6*, No. eaaz6844.
(26) Huang, Z.; Yao, Y.; Pang, Z.; Yuan, Y.; Li, T.; He, K.; Hu, X.; Cheng, J.; Yao, W.; Liu, Y.; Nie, A.; Sharifi-Asl, S.; Cheng, M.; Song, B.; Amine, K.; Lu, J.; Li, T.; Hu, L.; Shahbazian-Yassar, R. Direct Observation of the Formation and Stabilization of Metallic Nanoparticles on Carbon Supports. *Nat. Commun.* **2020**, *11*, 6373.
(27) Lee, Y.; Lee, J.; Chung, H.; Kim, J.; Lee, Z. In Situ Scanning Transmission Electron Microscopy Study of MoS 2 Formation on Graphene with a Deep-Learning Framework. *ACS Omega* **2021**, *6*, 21623−21630.
(28) Tamadoni Saray, M.; Yurkiv, V.; Shahbazian-Yassar, R. In Situ Thermolysis of a Ni Salt on Amorphous Carbon and Graphene Oxide Substrates. *Adv. Funct. Mater.* **2023**, 2213747.
(29) Perdew, J. P.; Ruzsinszky, A.; Csonka, G. I.; Vydrov, O. A.; Scuseria, G. E.; Constantin, L. A.; Zhou, X.; Burke, K. Restoring the Density-Gradient Expansion for Exchange in Solids and Surfaces. *Phys. Rev. Lett.* **2008**, *100*, 136406.
(30) Henkelman, G.; Uberuaga, B. P.; Jónsson, H. A Climbing Image Nudged Elastic Band Method for Finding Saddle Points and Minimum Energy Paths. *J. Chem. Phys.* **2000**, *113*, 9901−9904.
(31) Smidstrup, S.; Markussen, T.; Vancraeyveld, P.; Wellendorff, J.; Schneider, J.; Gunst, T.; Verstichel, B.; Stradi, D.; Khomyakov, P. A.; Vej-Hansen, U. G.; Lee, M. E.; Chill, S. T.; Rasmussen, F.; Penazzi, G.; Corsetti, F.; Ojanperä, A.; Jensen, K.; Palsgaard, M. L. N.; Martinez, U.; Blom, A.; Brandbyge, M.; Stokbro, K. QuantumATK: An Integrated Platform of Electronic and Atomic-Scale Modelling Tools. *J. Phys.: Condens. Matter* **2020**, *32*, 015901.
(32) Zhang, W.; Xu, H.; Xie, F.; Ma, X.; Niu, B.; Chen, M.; Zhang, H.; Zhang, Y.; Long, D. General Synthesis of Ultrafine Metal Oxide/Reduced Graphene Oxide Nanocomposites for Ultrahigh-Flux Nanofiltration Membrane. *Nat. Commun.* **2022**, *13*, 471.
(33) Park, S.; Lee, K.-S.; Bozoklu, G.; Cai, W.; Nguyen, S. T.; Ruoff, R. S. Graphene Oxide Papers Modified by Divalent Ions-Enhancing Mechanical Properties via Chemical Cross-Linking. *ACS Nano* **2008**, *2*, 572−578.
(34) Liu, X.; Ma, R.; Wang, X.; Ma, Y.; Yang, Y.; Zhuang, L.; Zhang, S.; Jehan, R.; Chen, J.; Wang, X. Graphene Oxide-Based Materials for Efficient Removal of Heavy Metal Ions from Aqueous Solution: A Review. *Environ. Pollut.* **2019**, *252*, 62−73.
(35) Ahmad, S. Z. N.; Wan Salleh, W. N.; Ismail, A. F.; Yusof, N.; Mohd Yusop, M. Z.; Aziz, F. Adsorptive Removal of Heavy Metal Ions Using Graphene-Based Nanomaterials: Toxicity, Roles of Functional Groups and Mechanisms. *Chemosphere* **2020**, *248*, 126008.
(36) Foroozan, T.; Soto, F. A.; Yurkiv, V.; Sharifi-Asl, S.; Deivanayagam, R.; Huang, Z.; Rojaee, R.; Mashayek, F.; Balbuena, P. B.; Shahbazian-Yassar, R. Synergistic Effect of Graphene Oxide for Impeding the Dendritic Plating of Li. *Adv. Funct. Mater.* **2018**, *28*, 1705917.
(37) Foroozan, T.; Yurkiv, V.; Sharifi-Asl, S.; Rojaee, R.; Mashayek, F.; Shahbazian-Yassar, R. Non-Dendritic Zn Electrodeposition Enabled by Zincophilic Graphene Substrates. *ACS Appl. Mater. Interfaces* **2019**, *11*, 44077−44089.
(38) Pelaez-Fernandez, M.; Bermejo, A.; Benito, A. M.; Maser, W. K.; Arenal, R. Detailed Thermal Reduction Analyses of Graphene Oxide via In-Situ TEM/EELS Studies. *Carbon* **2021**, *178*, 477−487.
(39) Leapman, R. D.; Grunes, L. A.; Fejes, P. L. Study of the L 23 Edges in the 3 d Transition Metals and Their Oxides by Electron-Energy-Loss Spectroscopy with Comparisons to Theory. *Phys. Rev. B* **1982**, *26*, 614−635.
(40) Bawane, K.; Manganaris, P.; Wang, Y.; Sure, J.; Ronne, A.; Halstenberg, P.; Dai, S.; Gill, S. K.; Sasaki, K.; Chen-Wiegart, Y. c. K.; Gakhar, R.; Mahurin, S.; Pimblott, S. M.; Wishart, J. F.; He, L. Determining Oxidation States of Transition Metals in Molten Salt Corrosion Using Electron Energy Loss Spectroscopy. *Scr. Mater.* **2021**, *197*, 113790.
(41) Gan, L.; Rudi, S.; Cui, C.; Strasser, P. Ni-Catalyzed Growth of Graphene Layers during Thermal Annealing: Implications for the Synthesis of Carbon-Supported Pt-Ni Fuel-Cell Catalysts. *ChemCatChem* **2013**, *5*, 2691−2694.
(42) Anton, R. On the Reaction Kinetics of Ni with Amorphous Carbon. *Carbon* **2008**, *46*, 656−662.
(43) Anton, R. In Situ TEM Investigations of Reactions of Ni, Fe and Fe−Ni Alloy Particles and Their Oxides with Amorphous Carbon. *Carbon* **2009**, *47*, 856−865.
(44) Rodríguez-Manzo, J. A.; Pham-Huu, C.; Banhart, F. Graphene Growth by a Metal-Catalyzed Solid-State Transformation of Amorphous Carbon. *ACS Nano* **2011**, *5*, 1529−1534.
(45) Schönecker, S.; Li, X.; Richter, M.; Vitos, L. Lattice Dynamics and Metastability of Fcc Metals in the Hcp Structure and the Crucial Role of Spin-Orbit Coupling in Platinum. *Phys. Rev. B* **2018**, *97*, 224305.
(46) Lin, H.; Liu, J.-X.; Fan, H.; Li, W.-X. Compensation between Surface Energy and Hcp/Fcc Phase Energy of Late Transition Metals from First-Principles Calculations. *J. Phys. Chem. C* **2020**, *124*, 11005−11014.
(47) Illy, S.; Tillement, O.; Machizaud, F.; Dubois, J. M.; Massicot, F.; Fort, Y.; Ghanbaja, J. First Direct Evidence of Size-Dependent Structural Transition in Nanosized Nickel Particles. *Philos. Mag. A* **1999**, *79*, 1021−1031.
(48) Tian, W.; Sun, H. P.; Pan, X. Q.; Yu, J. H.; Yeadon, M.; Boothroyd, C. B.; Feng, Y. P.; Lukaszew, R. A.; Clarke, R. Hexagonal Close-Packed Ni Nanostructures Grown on the (001) Surface of MgO. *Appl. Phys. Lett.* **2005**, *86*, 131915.
(49) Liang, J.; Ma, F.; Hwang, S.; Wang, X.; Sokolowski, J.; Li, Q.; Wu, G.; Su, D. Atomic Arrangement Engineering of Metallic Nanocrystals for Energy-Conversion Electrocatalysis. *Joule* **2019**, *3*, 956−991.
(50) Shin, H.-J.; Yoon, S.-M.; Mook Choi, W.; Park, S.; Lee, D.; Yong Song, I.; Sung Woo, Y.; Choi, J.-Y. Influence of Cu

https://doi.org/10.1021/acsanm.2c05528
ACS Appl. Nano Mater. 2023, 6, 10033−10043

Crystallographic Orientation on Electron Transport in Graphene. *Appl. Phys. Lett.* **2013**, *102*, 163102.
(51) Timonen, J. V. I.; Seppälä, E. T.; Ikkala, O.; Ras, R. H. A. From Hot-Injection Synthesis to Heating-Up Synthesis of Cobalt Nanoparticles: Observation of Kinetically Controllable Nucleation. *Angew. Chem.* **2011**, *123*, 2128−2132.
(52) Sharifi Dehsari, H.; Heidari, M.; Halda Ribeiro, A.; Tremel, W.; Jakob, G.; Donadio, D.; Potestio, R.; Asadi, K. Combined Experimental and Theoretical Investigation of Heating Rate on Growth of Iron Oxide Nanoparticles. *Chem. Mater.* **2017**, *29*, 9648−9656.
(53) van Embden, J.; Chesman, A. S. R.; Jasieniak, J. J. The Heat-Up Synthesis of Colloidal Nanocrystals. *Chem. Mater.* **2015**, *27*, 2246−2285.
(54) Li, Y.; Chen, Y.; Nie, A.; Lu, A.; Jacob, R. J.; Gao, T.; Song, J.; Dai, J.; Wan, J.; Pastel, G.; Zachariah, M. R.; Yassar, R. S.; Hu, L. In Situ, Fast, High-Temperature Synthesis of Nickel Nanoparticles in Reduced Graphene Oxide Matrix. *Adv. Energy Mater.* **2017**, *7*, 1601783.
(55) Chen, Y.; Egan, G. C.; Wan, J.; Zhu, S.; Jacob, R. J.; Zhou, W.; Dai, J.; Wang, Y.; Danner, V. A.; Yao, Y.; Fu, K.; Wang, Y.; Bao, W.; Li, T.; Zachariah, M. R.; Hu, L. Ultra-Fast Self-Assembly and Stabilization of Reactive Nanoparticles in Reduced Graphene Oxide Films. *Nat. Commun.* **2016**, *7*, 12332.
(56) Yao, Y.; Huang, Z.; Xie, P.; Wu, L.; Ma, L.; Li, T.; Pang, Z.; Jiao, M.; Liang, Z.; Gao, J.; He, Y.; Kline, D. J.; Zachariah, M. R.; Wang, C.; Lu, J.; Wu, T.; Li, T.; Wang, C.; Shahbazian-Yassar, R.; Hu, L. High Temperature Shockwave Stabilized Single Atoms. *Nat. Nanotechnol.* **2019**, *14*, 851−857.
(57) Scroccarello, A.; Álvarez-Diduk, R.; Della Pelle, F.; de Carvalho Castro e Silva, C.; Idili, A.; Parolo, C.; Compagnone, D.; Merkoçi, A. One-Step Laser Nanostructuration of Reduced Graphene Oxide Films Embedding Metal Nanoparticles for Sensing Applications. *ACS Sens.* **2023**, *8*, 598−609.
(58) Zhang, J.; Claverie, J.; Chaker, M.; Ma, D. Colloidal Metal Nanoparticles Prepared by Laser Ablation and Their Applications. *ChemPhysChem* **2017**, *18*, 986−1006.
(59) Chen, G.; Wang, F.; Liu, F.; Zhang, X. One-Pot Preparation of Ni-Graphene Hybrids with Enhanced Catalytic Performance. *Appl. Surf. Sci.* **2014**, *316*, 568−574.
(60) Ji, Z.; Shen, X.; Zhu, G.; Zhou, H.; Yuan, A. Reduced Graphene Oxide/Nickel Nanocomposites: Facile Synthesis, Magnetic and Catalytic Properties. *J. Mater. Chem.* **2012**, *22*, 3471−3477.
(61) Wei, L.; Mao, Y. Enhanced Hydrogen Storage Performance of Reduced Graphene Oxide Hybrids with Nickel or Its Metallic Mixtures Based on Spillover Mechanism. *Int. J. Hydrogen Energy* **2016**, *41*, 11692−11699.
(62) Shi, X.; Yu, J.; Liu, Q.; Shao, L.; Zhang, Y.; Sun, Z.; Huang, H. Metal-Organic-Framework-Derived N-P-and O-Codoped Nickel/Carbon Composites Homogeneously Decorated on Reduced Graphene Oxide for Energy Storage. *ACS Appl. Nano Mater.* **2020**, *3*, 5625−5636.
(63) Li, Y.; Huang, G.; Geng, Q.; Liu, Y.; Li, X.; Yao, Y.; Liu, Y.; Xing, B.; Liu, Q.; Jia, J.; Zhang, C. Nickel Salts-Induced Microstructure Modification of B−N Co-Doped Porous Carbons for High-Performance Supercapacitor Electrodes. *J. Alloys Compd.* **2022**, *895*, 162652.
(64) Niu, L.; Wang, J.; Hong, W.; Sun, J.; Fan, Z.; Ye, X.; Wang, H.; Yang, S. Solvothermal Synthesis of Ni/Reduced Graphene Oxide Composites as Electrode Material for Supercapacitors. *Electrochim. Acta* **2014**, *123*, 560−568.

https://doi.org/10.1021/acsanm.2c05528
ACS Appl. Nano Mater. 2023, 6, 10033−10043